Optical Engineering

OpticalEngineering.SPIEDigitalLibrary.org

Wave-optics investigation of turbulence thermal blooming interaction: II. Using time-dependent simulations

Mark F. Spencer

Mark F. Spencer, "Wave-optics investigation of turbulence thermal blooming interaction: II. Using time-dependent simulations," *Opt. Eng.* **59**(8), 081805 (2020), doi: 10.1117/1.OE.59.8.081805

Wave-optics investigation of turbulence thermal blooming interaction: II. Using time-dependent simulations

Mark F. Spencer[a,b,*]
[a]Air Force Research Laboratory, Directed Energy Directorate, Kirtland Air Force Base, New Mexico, United States
[b]Air Force Institute of Technology, Department of Engineering Physics, Wright-Patterson Air Force Base, Ohio, United States

Abstract. Part II of this two-part paper uses wave-optics simulations to look at the Monte Carlo averages associated with turbulence and time-dependent thermal blooming (TDTB). The goal is to investigate turbulence thermal blooming interaction (TTBI). At wavelengths near 1 μm, TTBI increases the amount of constructive and destructive interference (i.e., scintillation) that results from high-power laser beam propagation through distributed-volume atmospheric aberrations. As a result, we use the spherical-wave Rytov number, the number of wind-clearing periods, and the distortion number to gauge the strength of the simulated turbulence and TDTB. These parameters simply greatly given propagation paths with constant atmospheric conditions. In addition, we use the log-amplitude variance and the branch-point density to quantify the effects of TTBI. These metrics result from a point-source beacon being backpropagated from the target plane to the source plane through the simulated turbulence and TDTB. Overall, the results show that the log-amplitude variance and branch-point density increase significantly due to TTBI. This outcome poses a major problem for beam-control systems that perform phase compensation. [DOI: 10.1117/1.OE.59.8.081805]

Keywords: atmospheric propagation; atmospheric turbulence; thermal blooming; adaptive optics; beam control.

Paper 191816SS received Dec. 29, 2019; accepted for publication Mar. 9, 2020; published online Mar. 26, 2020.

1 Introduction

At wavelengths near 1 μm, the effects of turbulence are often more dominant than the effects of thermal blooming. Thus, at short-exposure time scales, one does not typically see fully formed crescent or half-moon irradiance patterns, as described in Fig. 1, due to thermal blooming at wavelengths near 1 μm. From a historical perspective, however, fully formed crescent or half-moon irradiance patterns do repeatedly result from the dominant effects of thermal blooming at wavelengths in the mid-wave and long-wave infrared.[1–5]

There is, nevertheless, an interaction that occurs between turbulence and thermal blooming at wavelengths near 1 μm.[6–10] This so-called turbulence thermal blooming interaction (TTBI), in practice, results in an increased amount of scintillation, which is the constructive and destructive interference that results from propagating high-power laser beams through distributed-volume atmospheric aberrations or "deep turbulence." In general, the scintillation caused by turbulence results in localized hot spots that cause localized heating of the atmosphere. This localized heating results in localized defocus-like optical effects (aka localized thermal blooming), which causes more constructive and destructive interference upon propagation through the atmosphere. Given weak-turbulence conditions, for example, the resulting scintillation caused by TTBI is often analogous to that experienced with deep-turbulence conditions. Therefore, thermal blooming can have a major impact on system performance (even at wavelengths near 1 μm).

---

*Address all correspondence to Mark F. Spencer, E-mail: mark.spencer@osamember.org

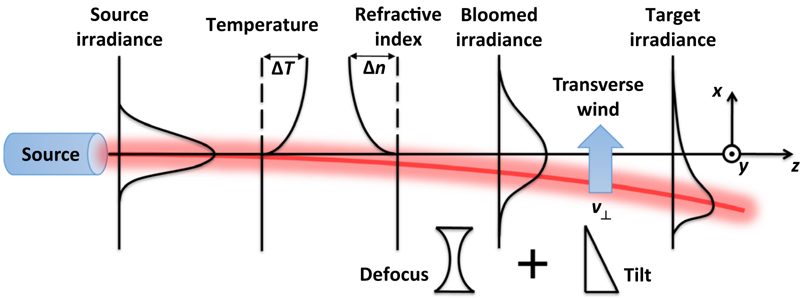

Fig. 1 Thermal blooming is a nonlinear optical effect caused by the irradiance (i.e., the power per unit area) of a high-power laser beam being absorbed by molecules and aerosols in the atmosphere. This absorbed irradiance leads to an increase in the temperature of the air and a decrease in the refractive index, creating a defocus-like optical effect that blooms the beam outward and decreases its peak irradiance. The presence of a transverse wind then contributes a tilt-like optical effect, which shifts the peak irradiance off target. After the wind has cleared through the source plane at least once, the conditions for static, whole-beam, or steady-state thermal blooming (SSTB) are generally met. The end result is a fully formed crescent or half-moon irradiance pattern in the target plane.

Beam-control (BC) systems, in theory, can mitigate the nonlinear optical effects induced by thermal blooming.[11] However, when one uses a single deformable mirror (DM) for phase-only compensation, analysis predicts the possibility of an instability due to positive feedback in the BC system.[12–16] Appropriately termed phase compensation instability (PCI), the positive feedback arises with the time-dependent development of scintillation within the propagating high-power laser beam. Recall that the localized hot spots produce defocus-like optical effects in the atmosphere. A BC system corrects for the hot spots by applying focus-like phase compensations. In turn, these phase compensations increase the strength of the localized thermal blooming, which leads to a runaway condition until something mitigates the positive feedback (e.g., wind variations in the atmosphere[17–21] or branch points in the phase function[22–26]).

Whether from TTBI or PCI, an increase in the amount of scintillation leads to an increase in the amount of total destructive interference, which leads to amplitude nulls in both the real and imaginary parts of the complex optical field. These amplitude nulls cause branch points and branch cuts (i.e., 2π discontinuities) to arise in the collimated phase function of a backpropagated beacon.[27,28] This outcome poses a major problem for BC systems that perform phase compensation. In practice, these branch points and branch cuts lead to fitting error in a BC system that uses a single continuous-face-sheet DM with a high-power coating for phase-only compensation.[29–33] With this last point in mind, the atmospheric propagation research community needs to quantify the impacts of TTBI and PCI using the larger grid sizes allowed by modern-day, wave-optics simulations.

The following is Part II of a two-part paper on TTBI performed using AOTools and WaveProp—both of which are MATLAB toolboxes written by the Optical Sciences Company.[34–38] In turn, this paper investigates TTBI in the presence of turbulence and time-dependent thermal blooming (TDTB). It does so via the Monte Carlo averages associated with the log-amplitude variance and the branch-point density. These metrics result from a point-source beacon being backpropagated from the target plane to the source plane through the simulated turbulence and TDTB. Part I of this two-part paper then investigates TTBI in the presence of turbulence and SSTB. Together, these papers will inform future wave-optics investigations.

It is important to note that this paper stands on its own as an independent article. However, it is also important to note that Part I of this two-part paper complements the analysis contained in this paper. In general, the steady-state assumptions contained in Part I allows us to explore the trade space in a computationally efficient manner, whereas the time-dependent assumptions contained in this paper allow us to examine the Monte Carlo averages with increased computational fidelity. For example, relative to the time-dependent results contained in this paper, the steady-state results contained in Part I provide an upper bound on both the increase in the log-amplitude variance and the branch-point density due to TTBI. Such results will hopefully prove fruitful in the development of next-generation scaling laws that account for the effects of TTBI.[39–45]

In what follows, Sec. 2 contains the setup for this paper, whereas Sec. 3 explores the trade space. Results and discussion then follow in Sec. 4, with a conclusion in Sec. 5. Before moving on to the next section, it is worth mentioning that this paper builds upon the preliminary analysis presented by Murphy and Spencer in a recent conference proceeding.[46] In particular, this paper develops time-dependent simulations with increased computational fidelity to clearly show an increase in both the log-amplitude variance and branch-point density due to TTBI. These results serve as a novel contribution to the atmospheric propagation research community.

2 Setup for the Wave-Optics Simulations

The desired setup is as follows. We wish to propagate a focused high-power laser beam with a wavelength of 1 μm along a propagation path with constant atmospheric conditions. Afterward, we wish to propagate a point-source beacon of the same wavelength back along the same path through the simulated turbulence and TDTB. For this purpose, we quickly review the details associated with the split-step beam propagation method (BPM), spherical-wave Rytov number, TDTB, number of wind-clearing periods, distortion number, and parameters of interest in the following sections. Given a common setup, this paper shares most of these sections with Part I of this two-part paper on TTBI. The analysis in this paper specifically differs in the sections on TDTB, number of wind-clearing periods, and parameters of interest. With that said, we include the shared sections in both papers for reading independence.

2.1 *Split-Step Beam Propagation Method*

In this paper, we make use of the commonly used split-step BPM, which simulates the propagation of monochromatic and polychromatic light through the atmosphere.[47–50] As described by Schmidt,[51] the split-step BPM divides the propagation path into independent volumes, with the atmospheric aberrations in each volume being represented by a single phase screen. The split-step BPM makes use of angular spectrum or plane-wave spectrum propagation to vacuum-propagate the light from a source plane to the first phase screen, applies the phase screen, and repeats this process until the monochromatic light reaches a target plane. Before moving on in the analysis, it is worth mentioning that AOTools and WaveProp make use of the split-step BPM. It is also worth mentioning that AOTools and WaveProp generate the phase screens associated with turbulence similar to the approach presented in Chapter 9 of Ref. 51. In this paper, we specifically use a Kolmogorov power-spectral density and do not add subharmonics or additional tilt to the generated phase screens.

2.2 *Spherical-Wave Rytov Number*

Provided the Rytov approximation, the propagation of a spherical wave through turbulence has an associated path-integral expression that serves as a gauge for the amount of scintillation.[41,51–54] Known as the spherical-wave Rytov number $\mathcal{R}_{\mathrm{sw}}$ (aka the spherical-wave Rytov parameter or spherical-wave, log-amplitude variance), this path-integral expression takes the following form:

$$\mathcal{R}_{\mathrm{sw}} = 0.563k^{7/6}\int_0^Z C_n^2(z)z^{5/6}\left(1-\frac{z}{Z}\right)^{5/6}\mathrm{d}z, \tag{1}$$

where $k = 2\pi/\lambda$ is the angular wavenumber, Z is the propagation distance, and $C_n^2(z)$ is the path-dependent refractive index structure coefficient. Given propagation paths with constant atmospheric conditions, this path-integral expression reduces to the following closed-form expression:

$$\mathcal{R}_{\mathrm{sw}} = 0.124k^{7/6}C_n^2Z^{11/6}. \tag{2}$$

For all intents and purposes, the strong scintillation regime occurs when $\mathcal{R}_{\mathrm{sw}}$ is greater than 0.25. This regime is where the Rytov approximation readily breaks down with respect to the log-amplitude fluctuations[52,53] and branch points and branch cuts (i.e., 2π discontinuities) readily show up in the phase function.[27,28] Thus, in the analysis that follows, we will use $\mathcal{R}_{\mathrm{sw}}$ as a gauge for the strength of the simulated turbulence.

2.3 *Time-Dependent Thermal Blooming*

The heating of the atmosphere due to an absorbed irradiance is balanced by the cooling of the atmosphere due to a transverse wind blowing across the high-power laser beam. Mathematically, we realize this heating and cooling via a forced-advection equation, such that

$$\frac{\partial}{\partial t}\Delta n(\mathbf{r},t)+\mathbf{v}_{\perp}(z)\cdot\nabla_{\perp}\Delta n(\mathbf{r},t)=-\mu(z)i_{\mathrm{HP}}(\mathbf{r},t). \tag{3}$$

Here, $\partial/\partial t$ is the partial-derivative operator with respect to time, $\Delta n(\mathbf{r},t)$ is the position- and time-dependent change in the refractive index, $\mathbf{v}_{\perp}(z)=v_x(z)\hat{\mathbf{x}}+v_y(z)\hat{\mathbf{y}}$ is the path-dependent transverse wind velocity vector, $\nabla_{\perp}=\partial/\partial x\hat{\mathbf{x}}+\partial/\partial y\hat{\mathbf{y}}$ is the transverse-gradient operator,

$$\mu(z)=\frac{[n_0(z)-1]\alpha(z)}{C_P(z)\rho_0(z)T_0(z)} \tag{4}$$

is the path-dependent absorbed irradiance coefficient, $n_0(z)$ is the path-dependent ambient refractive index, $\alpha(z)$ is the path-dependent absorption coefficient, $C_P(z)$ is the path-dependent specific heat at constant pressure, $\rho_0(z)$ is the path-dependent density of air at constant pressure, $T_0(z)$ is the path-dependent ambient temperature, and $i_{\mathrm{HP}}(\mathbf{r},t)$ is the position- and time-dependent, high-power laser beam irradiance. For all intents and purposes, Eq. (3) says that the energy acquired in heating the atmosphere due to an absorbed irradiance $\mu(z)i_{\mathrm{HP}}(\mathbf{r},t)$ is balanced by a loss of energy due to cooling from a transverse wind velocity vector $\mathbf{v}_{\perp}(z)$ blowing across the high-power laser beam. As a result, the thermal blooming literature often refers to Eq. (3) as the energy-balance equation.

It is informative to determine the impulse response to the energy-balance equation. For this purpose, we rewrite Eq. (3) in operator form as

$$\boldsymbol{\mathcal{L}}\{\Delta n(x,y,z,t)\}=-f(x,y,z,t), \tag{5}$$

where $\mathcal{L}\{\odot\}=[\partial/\partial t+\mathbf{v}_{\perp}(z)\cdot\nabla_{\perp}]\odot$ is a linear operator that represents cooling of the atmosphere and $f(x,y,z,t)=\mu(z)i_{\mathrm{HP}}(\mathbf{r},t)$ is a forcing function that represents heating of the atmosphere. Now, we can make use of a Green's function analysis, such that

$$\boldsymbol{\mathcal{L}}\{G(x,y,z,t;\xi,\eta,\zeta,\tau)\}=-\delta(x-\xi,y-\eta,z-\zeta,t-\tau), \tag{6}$$

where here we replace $\Delta n(\mathbf{r},t)$ with a Green's function or impulse response, $G(x,y,z,t;\xi,\eta,\zeta,\tau)$, and $f(x,y,z,t)$ with a shifted Dirac-delta or impulse function, $\delta(x-\xi,y-\eta,z-\zeta,t-\tau)$. We can also account for the change in the refractive index $\Delta n(\mathbf{r},t)$ using the following superposition integral:

$$\Delta n(x,y,z,t)=\int_{-\infty}^{\infty}\int_{-\infty}^{\infty}\int_{-\infty}^{\infty}\int_{-\infty}^{\infty}G(x,y,z,t;\xi,\eta,\zeta,\tau)f(\xi,\eta,\zeta,\tau)\mathrm{d}\xi\,\mathrm{d}\eta\,\mathrm{d}\zeta\,\mathrm{d}\tau. \tag{7}$$

Thus, we need to determine $G(x,y,z,t;\xi,\eta,\zeta,\tau)$ to determine $\Delta n(\mathbf{r},t)$.

To determine the Green's function $G(x,y,z,t;\xi,\eta,\zeta,\tau)$ needed in Eq. (7), we can use a two-dimensional (2-D) Fourier transformation and a unilateral Laplace transformation to transform Eq. (6) into an algebraic expression. If we assume that there is no initial heating of the atmosphere, then we can easily solve for the Green's function in the frequency domain. Afterward, we can use a 2-D inverse Fourier transformation and an inverse Laplace transformation to transform back into the spatial and temporal domains, so that

$$\begin{aligned} G(x,y,z,t;\xi,\eta,\zeta,\tau) &= G(x-\xi,y-\eta,z-\zeta,t-\tau) \\ &= -\delta[x-\xi+v_x(z)(t-\tau),y-\eta-v_y(z)(t-\tau),z-\zeta]\mathrm{step}(t-\tau). \end{aligned} \tag{8}$$

Here, $\mathrm{step}(x)$ is a unit-step or Heaviside function, such that

$$\mathrm{step}(x) = \begin{cases} 1 & x > 0 \\ 1/2 & x = 0 \\ 0 & x < 0 \end{cases}. \tag{9}$$

If we substitute Eq. (8) into Eq. (7), we can account for the effects of TDTB. With a little manipulation, we determine the change in the refractive index $\Delta n(\mathbf{r},t)$ as

$$\Delta n(x,y,z,t) = -\mu(z)\int_0^t i_{\mathrm{HP}}[x-v_x(z)(t-\tau),y-v_y(z)(t-\tau),z,\tau]\mathrm{d}\tau. \tag{10}$$

It is readily seen from Eq. (10) that as time t progresses from some previous time τ, $\Delta n(\mathbf{r},t)$ decreases. This outcome results in a defocus-like optical effect in the atmosphere. It is also readily seen from Eq. (10) that the transverse wind velocity vector $\mathbf{v}_\perp(z)$ with components $v_x(z)$ and $v_y(z)$ in the $\hat{\mathbf{x}}$ and $\hat{\mathbf{y}}$ directions, respectively, causes the peak irradiance to spatially shift. This outcome causes a tilt-like optical effect in the atmosphere. Recall that we can visualize both of these effects in Fig. 1.

We can account for the effects of TDTB using AOTools and WaveProp, since these MATLAB toolboxes solve the integral expression found in Eq. (10) numerically.[34–38] In particular, AOTools and WaveProp updates the change in the refractive index $\Delta n(\mathbf{r},t)$ from a previous time step t_j to the present time step t_{j+1} with the time step $\Delta t = t_{j+1} - t_j$, viz.

$$\Delta n(x,y,z,t_{j+1}) = -\mu(z)i_{\mathrm{HP}}(x,y,z,t_{j+1})\Delta t + \Delta n[x-v_x(z)\Delta t,y-v_y(z)\Delta t,z,t_j]. \tag{11}$$

The heating of the atmosphere at the present time step t_{j+1} corresponds to the amount of absorbed irradiance, $\mu(z)i_{\mathrm{HP}}(x,y,z,t_{j+1})$, and Eq. (11) deposits this heat during the time step Δt. The cooling of the atmosphere at the previous time step t_j then corresponds to amount of transverse wind, $v_x(z)$ and $v_y(z)$, blowing across the high-power laser beam, and Eq. (11) removes this heat during the time step Δt. Thus, the heating of the atmosphere due to an absorbed irradiance is balanced by the cooling of the atmosphere due to a transverse wind.

When using $N \times N$ grids to implement Eq. (11) into wave-optics simulations, it is important to note that the amount of spatial shift is often less than or greater than the grid sampling δ. As a result, it is common practice to break the time development of Eq. (11) into subtime steps.[35,36] Waveprop and AOTools subsequently uses linear interpolation for each subspatial shift. It is also important to note that when assuming Taylor's frozen flow, time-dependent turbulence satisfies an unforced version of Eq. (3). As a result, WaveProp and AOTools uses Eq. (11), without the first term on the right-hand side of the equals sign, to simulate the effects of time-dependent turbulence.

2.4 *Number of Wind-Clearing Periods*

In this paper, we define the wind-clearing time, t_0, as the period of time needed for the initial transverse wind speed, $|\mathbf{v}_\perp(0)| = v_0$ (in the source plane at $z = 0$), to travel across the initial diameter, D_0, where

$$t_0 = \frac{D_0}{v_0}. \tag{12}$$

If there are no variations in the exitance of the focused high-power laser beam and ambient atmosphere, then TDTB can reach a steady state with a fully formed crescent or half-moon irradiance pattern in the target plane (cf. Fig. 1). Different parameters of interest (cf. the next section) require different multiples of t_0 for TDTB to reach a true steady state. As such, we define multiples of t_0 in terms of a parameter referred to here as the number of wind-clearing periods N_{WCP}. Moving forward we will use N_{WCP} as a gauge for how much the wind transverses D_0.

After the wind transverses the initial diameter D_0 at least once (when $N_{\mathrm{WCP}} \geq 1$), the conditions for SSTB are generally met. In practice, SSTB results in a static behavior of the change in the refractive index. This static behavior causes the time rate of change of the change in the refractive index to be zero. Consequently, we drop any time dependence, and the position-dependent change in the refractive index $\Delta n(\mathbf{r})$ due to SSTB results as

$$\Delta n(\mathbf{r}) = \Delta n(x, y, z) = -\frac{\mu(z)}{v_\perp(z)} \int_{-\infty}^{x} i_{\mathrm{HP}}(\xi, y, z)\mathrm{d}\xi. \tag{13}$$

In writing Eq. (13), we assume that the transverse wind velocity is solely in the x direction, hence the limits of integration. We will use this assumption in the following analysis [i.e., $\mathbf{v}_\perp(z) = v_\perp(z)\hat{\mathbf{x}} + 0\hat{\mathbf{y}}$].

2.5 *Distortion Number*

It is useful to describe the refraction caused by SSTB in terms of a phase error $\phi(x, y, Z)$ measured in radians. For this purpose,

$$\phi(x, y, Z) = k \int_0^Z \Delta n(x, y, z)\mathrm{d}z, \tag{14}$$

where again $k = 2\pi/\lambda$ is the angular wavenumber and Z is the propagation distance. Substituting Eq. (13) into Eq. (14) results in the following relationship:

$$\phi(x, y, Z) = -k \int_0^Z \frac{\mu(z)}{v_\perp(z)} \int_{-\infty}^{x} i_{\mathrm{HP}}(\xi, y, z)\mathrm{d}\xi\, \mathrm{d}z. \tag{15}$$

As shown in Eq. (15), we can characterize the radians of distortion induced by SSTB.

For focused high-power laser beams with initial power, P_0, and initial diameter, D_0, we can rewrite Eq. (15) in terms of a path-integral expression known as the distortion number, N_D. In particular,

$$\phi(x, y, Z) \approx -N_D \frac{D_0}{4\sqrt{2}P_0} \int_{-\infty}^{x} i_{\mathrm{HP}}(\xi, y, 0)\mathrm{d}\xi \tag{16}$$

and

$$N_D = 4\sqrt{2}P_0 k \int_0^Z \frac{Z - z}{Z} \frac{\mu(z)\tau(z)}{D(z)v_\perp(z)} \mathrm{d}z. \tag{17}$$

From the source plane at $z = 0$ to the target plane at $z = Z$, the optical leverage $(Z - z)/Z$ causes D_0 to converge upon propagation so that

$$D(z) = \frac{Z - z}{Z} D_0 \tag{18}$$

is the path-dependent beam diameter from geometrical or ray optics. Note that we include the path-dependent transmittance $\tau(z)$, such that

$$\tau(z) = \exp\left[-\int_0^z \kappa(\zeta)\mathrm{d}\zeta\right], \tag{19}$$

in the definition of N_D because of extinction effects from the path-dependent extinction coefficient $\kappa(z) = \alpha(z) + \sigma(z)$, where $\sigma(z)$ is the path-dependent scattering coefficient. In turn, N_D provides a gauge for the radians of distortion induced by SSTB.

Given propagation paths with constant atmospheric conditions, Eq. (17) simplifies, such that

$$N_D = \frac{4\sqrt{2}P_0 k(n_0 - 1)\alpha \mathrm{e}^{-\alpha Z}\mathrm{e}^{-\sigma Z} Z}{C_P \rho_0 T_0 D_0 v_\perp}. \tag{20}$$

For all intents and purposes, the strong-distortion regime occurs when the distortion number N_D is greater than the critical number $N_C = 16\sqrt{2} \approx 22.6$.[34] This regime is where the radians of distortion induced by SSTB give rise to significant fluctuations in the fully formed crescent or half-moon irradiance pattern (cf. Fig. 1). Thus, in the analysis that follows, we will use N_D as a gauge for the strength of the simulated TDTB.

2.6 *Parameters of Interest*

Table 1 contains all the parameters of interest in the wave-optics simulations. It is important to note that the wave-optics simulations used $N \times N$ grids. The side length S was the same in both the source and target planes creating unity scaling within the wave-optics simulations. By choice, the wave-optics simulations also satisfied Fresnel scaling, such that $N = S^2/(\lambda Z)$, where λ is the wavelength and Z is the propagation distance. The resulting $N \times N$ grid also minimized the effects of aliasing without making the wave-optics simulations too computationally expensive.

In addition to Fresnel scaling, we ensured that the wave-optics simulations had at least 10 pixels across the spherical-wave Fried parameter $r_{0,\mathrm{sw}}$ (aka the spherical-wave coherence diameter or spherical-wave coherence length).[41,51–54] Given a propagation path with constant atmospheric conditions, the associated path-integral expression simplifies into the following closed-form expression:

$$r_{0,\mathrm{sw}} = \left[0.423k^2 \int_0^Z C_n^2(z)\left(\frac{z}{Z}\right)^{5/3} \mathrm{d}z\right]^{-3/5} \Rightarrow r_{0,sw} = (0.159k^2 C_n^2 Z)^{-3/5}. \tag{21}$$

Table 1 Parameters of interest in the wave-optics simulations.

Parameters (MKS units)	Symbol	Value(s)
Grid	$N \times N$	1024×1024
Side length (m)	S	2.263
Wavelength (m)	λ	1×10^{-6}
Propagation distance (m)	Z	5000
Distortion number (rad)	N_D	$16\sqrt{2}$
Initial power (kW)	P_0	125.4
Ambient refractive index difference	$(n_0 - 1)$	2.602×10^{-4}
Absorption coefficient (m^{-1})	α	5×10^{-6}
Scattering coefficient (m^{-1})	σ	5×10^{-5}
Specific heat at constant pressure (J/kg/K)	C_P	1004
Density of air at constant pressure ($\mathrm{kg/m^3}$)	ρ_0	1.293
Ambient temperature (K)	T_0	300
Transverse wind speed (m/s)	$v_\perp$	5

Table 2 Turbulence scenario used in the wave-optics simulations. Recall that C_n^2 is the refractive index structure coefficient, $\mathcal{R}_{\mathrm{sw}}$ is the spherical-wave Rytov number, D_0 is the aperture diameter, $r_{0,\mathrm{sw}}$ is the spherical-wave Fried parameter, θ_0 is the isoplanatic angle, λ/D_0 is the diffraction-limited angle, and f_G is the Greenwood frequency.

Scenario	$\mathcal{R}_{\mathrm{sw}}$	C_n^2 ($\mathrm{m}^{-2/3}$)	$D_0/r_{0,\mathrm{sw}}$	$\theta_0/(\lambda/D_0)$	f_G (Hz)
1	0.25	0.391×10^{-14}	8.96	1.75	68.6

Table 2 makes use of this closed-form expression in defining the turbulence scenario used in the wave-optics simulations. For completeness in defining the turbulence scenarios,[41,51–54] it also makes use of the isoplanatic angle, θ_0, and the Greenwood frequency, f_G, such that

$$\theta_0 = \left[2.91k^2 \int_0^Z C_n^2(z)(Z-z)^{5/3}\mathrm{d}z\right]^{-3/5} \Rightarrow \theta_0 = 0.314\frac{r_{0,\mathrm{sw}}}{Z} \tag{22}$$

and

$$f_G = \left[0.102k^2 \int_0^Z C_n^2(z)v_\perp(z)^{5/3}\mathrm{d}z\right]^{3/5} \Rightarrow f_G = (0.102k^2 C_n^2 v^{5/3} Z)^{3/5}. \tag{23}$$

Notice that the scenarios defined in Table 2 include a spherical-wave Rytov number $\mathcal{R}_{\mathrm{sw}}$ of 0.25, right at the demarcation of the strong-scintillation regime (when $\mathcal{R}_{\mathrm{sw}} > 0.25$). Also notice that the scenarios defined in Table 1 include a distortion number N_D of $16\sqrt{2}$, right at the demarcation of the strong distortion regime (when $N_D > N_C = 16\sqrt{2} \approx 22.6$). With these regimes in mind, we will explore the overall trade space in the next section.

Before moving on to the next section, it is important to note that we used the Greenwood frequency f_G (rounded to one significant figure) to determine the time step Δt needed in the wave-optics simulations. In particular,

$$\Delta t = \frac{1}{20 f_G} = 0.714\ \mathrm{ms}. \tag{24}$$

This choice allowed us to satisfy the 20× rule of thumb used in the design of closed-loop BC systems (i.e., the sampling frequency should be 20× the disturbance frequency to obtain good closed-loop performance). Such a choice might inform future PCI investigations using wave-optics simulations.

3 Exploration Using the Wave-Optics Simulations

In this section, we make use of the wave-optics simulations setup in the previous section to explore the trade space. The goal is to investigate TTBI in terms of the normalized power in the bucket (PIB), P_N, and the peak Strehl ratio, S_P, associated with a focused high-power laser beam being propagated from the source plane at $z = 0$ to the target plane at $z = Z$, and the log-amplitude variance, σ_χ^2, and the branch-point density, $\mathcal{D}_{\mathrm{BP}}$, associated with a point-source beacon being backpropagated from the target plane at $z = Z$ to the source plane $z = 0$. Here,

$$P_N = \frac{\int_{-\infty}^{\infty} \mathrm{cyl}\left(\frac{\sqrt{x^2+y^2}}{D_Z}\right) i_{\mathrm{HP}}(x,y,Z)\mathrm{d}x\,\mathrm{d}y}{P_0}, \tag{25}$$

$$S_P = \frac{\max\{i_{\mathrm{HP}}(x,y,Z)\}}{i_{\mathrm{DL}}(0,0,Z)}, \tag{26}$$

$$\sigma_\chi^2 = \mathrm{var}[\chi_{\mathrm{PS}}(x,y,0)], \tag{27}$$

and

$$\mathcal{D}_{\mathrm{BP}} = \frac{N_{\mathrm{BP}}}{\pi(D_0/2)^2}. \tag{28}$$

In Eqs. (25)–(28), $\mathrm{cyl}(\rho)$ is the cylinder function, such that

$$\mathrm{cyl}(\rho) = \begin{cases} 1 & 0 \le \rho < 1/2 \\ 1/2 & \rho = 1/2 \\ 0 & \rho > 1/2 \end{cases}; \tag{29}$$

$D_Z = 2.44\lambda Z/D_0$ is the diffraction-limited bucket diameter; $i_{\mathrm{HP}}(x, y, Z)$ is the focused high-power laser beam irradiance in the target plane; P_0 is again the initial power; $\max\{\odot\}$ is an operator that computes the maximum value; $i_{\mathrm{DL}}(0,0,Z)$ is the focused on-axis, diffraction-limited, high-power laser beam irradiance in the target plane; $\mathrm{var}\{\odot\}$ is an operator that computes the spatial variance; $\chi_{\mathrm{PS}}(x, y, 0) = \ln\{|U_{\mathrm{PS}}(x, y, 0)|\}$ is the log amplitude of the backpropagated point-source beacon in the source plane; N_{BP} is the number of branch points in the collimated phase function of the backpropagated point-source beacon; and D_0 is again the initial diameter.

To calculate the number of branch points N_{BP} in Eq. (28), we used the following relationship:

$$\oint_C \nabla\phi(x, y, 0) \cdot \mathrm{d}\mathbf{r} = \pm 2\pi(N_+ - N_-), \tag{30}$$

where N_+ is the number of positively charged branch points and N_- is the number of negatively charged branch points within the collimated phase function $\phi(x, y, 0)$. This relationship says that we can determine the location of a branch point when the line integral around the closed curve C of the gradient of the collimated phase function $\nabla\phi(x, y, 0)$ does not equal zero, specifically, where $\nabla\phi(x, y, 0)$ is a nonconservative vector field. To account for this relationship numerically, AOTools and WaveProp discretely samples the continuous integral in Eq. (30) by breaking the $N \times N$ grid into a bunch of 2×2 subgrids and summing up the phase derivative around each point. A positive 2π value results in a positively charged branch point and a negative 2π value results in a negatively charged branch point. In turn, to calculate N_{BP}, we computed the sum of the total number of positive and negative branch points associated with the pixels found within $\phi(x, y, 0)$.

In what follows, we will use the metrics defined in Eqs. (25)–(28) to visualize the following topics:

1. the number of wind-clearing periods needed to simulate the effects of TDTB,
2. the focused high-power laser beam in the target plane,
3. the backpropagated point-source beacon in the source plane, and
4. the overall trade space in terms of the normalized PIB, P_N, and the peak Strehl ratio, S_P.

Each topic is the subject of the following sections. These sections will inform the results and discussion presented in Sec. 4.

3.1 *Number of Wind-Clearing Periods Needed*

To determine the number of wind-clearing periods, N_{WCP}, needed to accurately simulate TDTB using the split-step BPM, we calculated both the normalized PIB, P_N, and the peak Strehl ratio, S_P, as a function of N_{WCP}. In addition, we calculated P_N and S_P assuming SSTB conditions. Figure 2 shows the outcomes of these calculations. As shown, we can see that both P_N and S_P reach steady state (accurate to the third decimal place) when $N_{\mathrm{WCP}} \ge 1$. Thus, in the analysis that follows, we used $N_{\mathrm{WCP}} = 2$ to simulate the effects of TDTB.

Note that we used 50 equally spaced phase screens to simulate the effects of both TDTB and SSTB in Fig. 2. In general, this choice was accurate to the third decimal place (cf. Fig. 2 in Part I). For convenience in the wave-optics simulations, we also used 50 equally spaced phase screens to simulate the effects of turbulence. Therefore, in the analysis that follows,

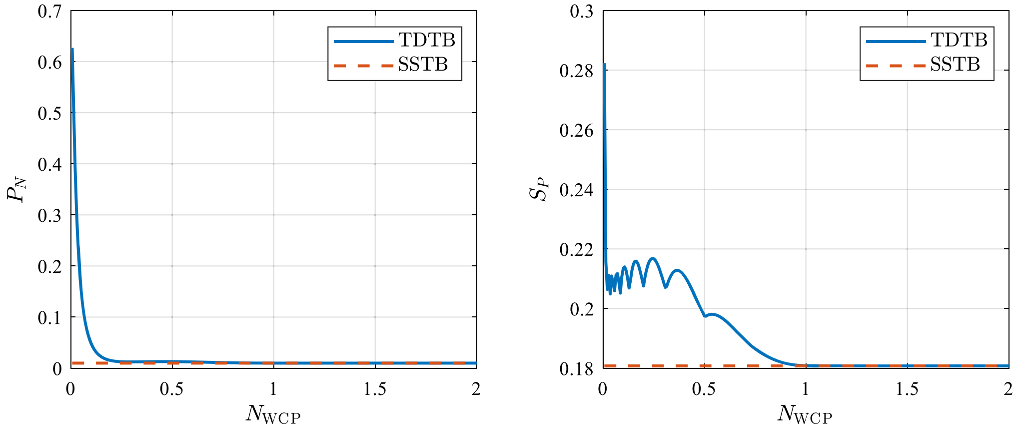

(a)

(b)

Fig. 2 Visualization of the number of wind-clearing periods N_{WCP} needed to simulate the effects of TDTB: (a) the normalized PIB P_N and (b) the peak Strehl ratio S_P. Note that P_N and S_P reach steady state when NWCP = 1.

the phase screens used for simulating turbulence and TDTB (using the split-step BPM) were collocated along the propagation path. This choice led to small percentage errors (less than a 10th of a percentage) between the continuous and discrete calculations of the parameters found in Table 2.[51]

3.2 *Focused High-Power Laser Beam*

To create the focused high-power laser beam, we used a series of steps starting with the creation of a positive thin lens transmittance function of circular diameter D_0 and focus Z. Assuming plane-wave illumination, we then set the exitance i_0 of the focused high-power laser beam, such that $i_0 = 4P_0/(\pi D_0^2)$. This series of steps created a top-hat or flat-top beam profile in the source plane with approximately 256 grid points across D_0. As discussed above, AOTools and WaveProp then used the split-step BPM to propagate the focused high-power laser beam from the source plane to the target plane.

Based on previously published theoretical explorations,[6–10] we hypothesized that the simulated turbulence and TDTB would increase the amount of scintillation found in a propagated high-power laser beam due to TTBI. In turn, the normalized PIB P_N and peak Strehl ratio S_P for the TTBI case would typically decrease in comparison to the simulated diffraction-limited, turbulence-only, and TDTB-only cases. Figure 3 demonstrates this hypothesis to be true for one Monte Carlo realization, where $\mathcal{R}_{\mathrm{sw}} = 0.25$, $N_{\mathrm{WCP}} = 1$, and $N_D = N_C = 16\sqrt{2} \approx 22.6$ [cf. Eqs. (2), (12), and (20), respectively]. Notice that we report values for both P_N and S_P at the top of each normalized irradiance subplot in Fig. 3. Also notice that these irradiance subplots are similar but different to those reported in Part I using steady-dependent simulations (cf. Fig. 3 in Part I) since both papers use the same Monte Carlo realization of turbulence.

3.3 *Backpropagated Point-Source Beacon*

To create the backpropagated point-source beacon, AOTools and WaveProp used a series of steps starting with the creation of a positive thin lens transmittance function of square width $2D_0$ and focus Z. Assuming Fresnel scaling, AOTools and WaveProp vacuum-propagated this positive thin lens transmittance function from the source plane to the target plane using angular spectrum or plane-wave spectrum propagation. This series of steps created a sinc-like function in the target plane with three pixels across its central lobe. As discussed above, AOTools and WaveProp then used the split-step BPM to backpropagate the point-source beacon from the target plane to the source plane.

Again, based on previously published theoretical explorations,[6–10] we hypothesized that the simulated turbulence and TDTB would increase the amount of scintillation found in a

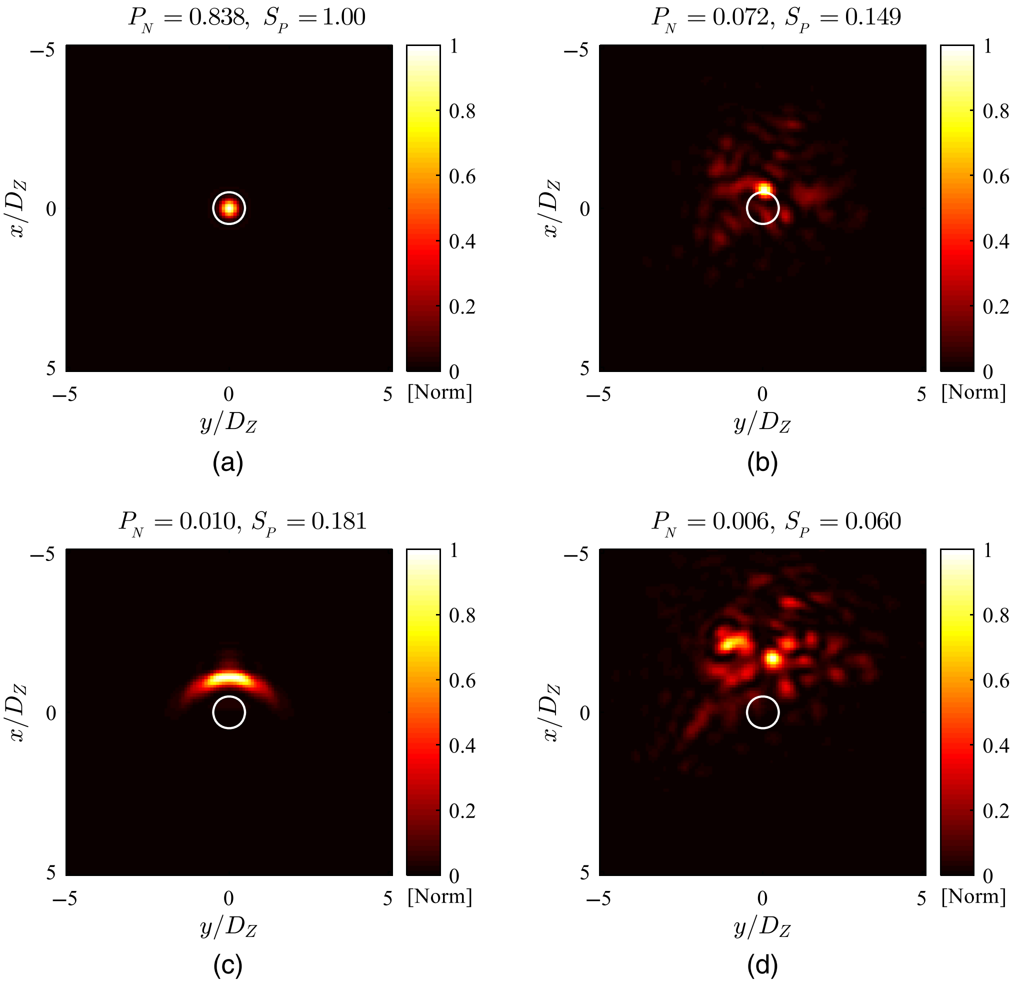

Fig. 3 Visualization of the focused high-power laser beam in the target plane. Here, we plot the normalized irradiance associated with (a) the diffraction-limited case, (b) the turbulence-only case, (c) the TDTB-only case, and (d) the TTBI case. We also report the normalized PIB P_N and the peak Strehl ratio S_P at the top of each subplot. Note that the white circles represent the diffraction-limited bucket diameter D_Z.

backpropagated point-source beacon due to TTBI. As a result, the log-amplitude variance σ_χ^2 and branch-point density $\mathcal{D}_{\mathrm{BP}}$ for the TTBI case would typically increase in comparison to the simulated diffraction-limited, turbulence-only, and TDTB-only cases. Figures 4 and 5 demonstrate this hypothesis to be true for one Monte Carlo realization, where $\mathcal{R}_{\mathrm{sw}} = 0.25$, $N_{\mathrm{WCP}} = 1$, and $N_D = N_C = 16\sqrt{2} \approx 22.6$ [cf. Eqs. (2), (12), and (20), respectively]. Notice that we report values for both σ_χ^2 and $\mathcal{D}_{\mathrm{BP}}$ at the top of each normalized irradiance subplot in Fig. 4 and each wrapped phase subplot in Fig. 5. Also notice that these irradiance subplots are similar but different to those reported in Part I using steady-state simulations (cf. Figs. 4 and 5 in Part I) since both papers use the same Monte Carlo realization of turbulence.

To further explore the effects of TTBI, we also calculated the irrotational phase estimate, $\hat{\phi}_{\mathrm{irr}}(x, y, 0)$, and rotational phase estimate, $\hat{\phi}_{\mathrm{rot}}(x, y, 0)$. Figure 6 shows these estimates. In practice, these estimates originated from the collimated phase functions $\phi(x, y, 0)$ found in Figs. 5(b) and 5(d), for the turbulence-only and TTBI cases, respectively. To calculate $\hat{\phi}_{\mathrm{irr}}(x, y, 0)$ and $\hat{\phi}_{\mathrm{rot}}(x, y, 0)$ from $\phi(x, y, 0)$, we used the following relationships:[27–31]

$$\hat{\phi}_{\mathrm{irr}}(x, y, 0) = \mathrm{LS}\{\phi(x, y, 0)\} = \phi_{\mathrm{LS}}(x, y, 0) \tag{31}$$

and

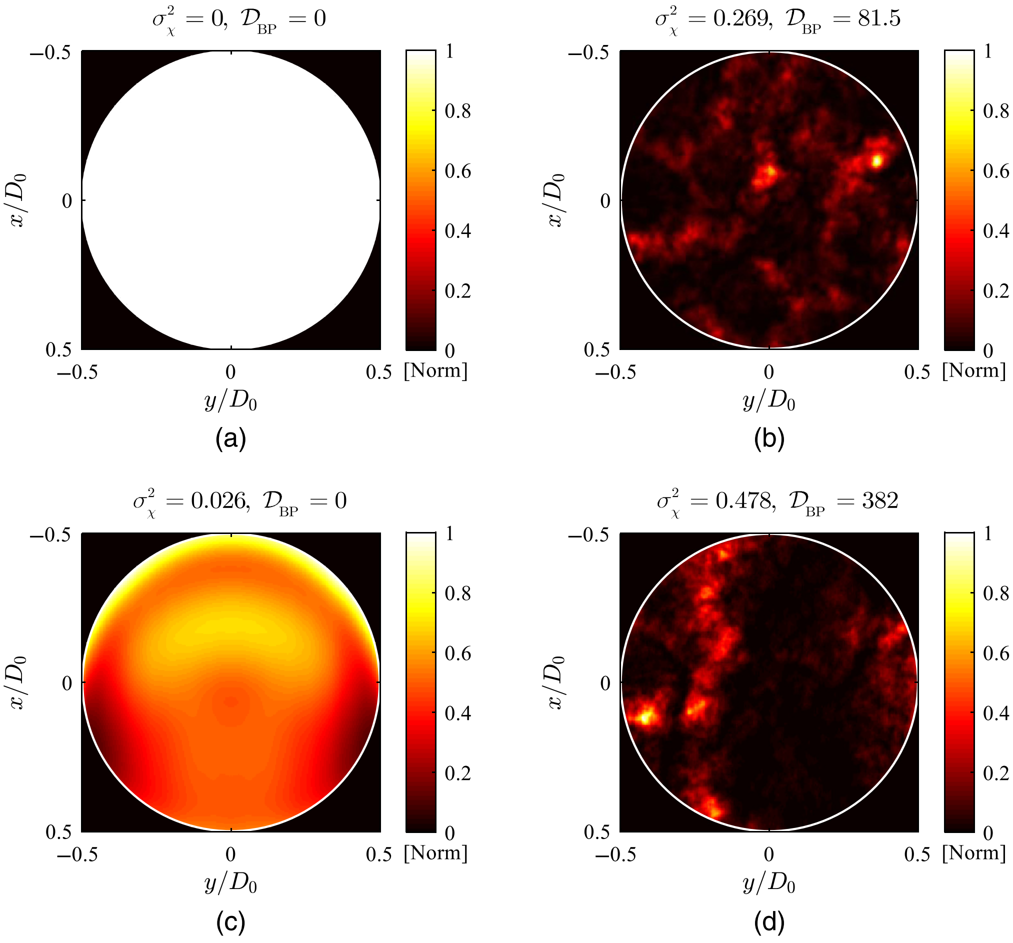

Fig. 4 Visualization of the backpropagated point-source beacon in the source plane. Here, we plot the normalized irradiance associated with (a) the diffraction-limited case, (b) the turbulence-only case, (c) the TDTB-only case, and (d) the TTBI case. Similar to Figs. 5 and 6, we also report the log-amplitude variance σ_χ^2 and the branch-point density $\mathcal{D}_{BP}$ at the top of each subplot. Note that the white circles represent the initial diameter D_0.

$$\hat{\phi}_{\mathrm{rot}}(x, y, 0) = \arg\{\exp(j[\phi(x, y, 0) - \phi_{\mathrm{LS}}(x, y, 0)])\}, \tag{32}$$

where $\mathrm{LS}\{\odot\}$ is an operator that unwraps the phase using a least-squares algorithm and $\arg\{\odot\}$ is an operator that extracts the wrapped phase ϕ from a phasor of the form $\exp[j\phi]$.

Figure 6 shows that both the irrotational phase estimate, $\hat{\phi}_{\mathrm{irr}}(x, y, 0)$, and the rotational phase estimate, $\hat{\phi}_{\mathrm{rot}}(x, y, 0)$, contain more phase features due to the TTBI case [cf. Figs. 6(b) and 6(d)] compared to the turbulence-only case [cf. Figs. 6(a) and 6(c)]. This outcome says that a BC system, in general, will need more resolution and stroke to correct for $\hat{\phi}_{\mathrm{irr}}(x, y, 0)$. It also says that $\hat{\phi}_{\mathrm{rot}}(x, y, 0)$ will lead to an increased amount of fitting error because of the 2π discontinuities associated with branch points and branch cuts, especially when using a single continuous-face-sheet DM with a high-power coating for phase-only compensation.[29–33]

3.4 *Overall Trade Space*

Figure 7 shows the overall trade space in terms of the normalized PIB, P_N, and the peak Strehl ratio, S_P. Here, we calculated both metrics as a function of the number of wind-clearing periods N_{WCP}. As N_{WCP} increases, both P_N and S_P decrease, which makes good sense. Note that the bold curves report the averages and the light curves report the standard deviations associated with 100 Monte Carlo realizations. Also note that the widths of these light curves are reasonably

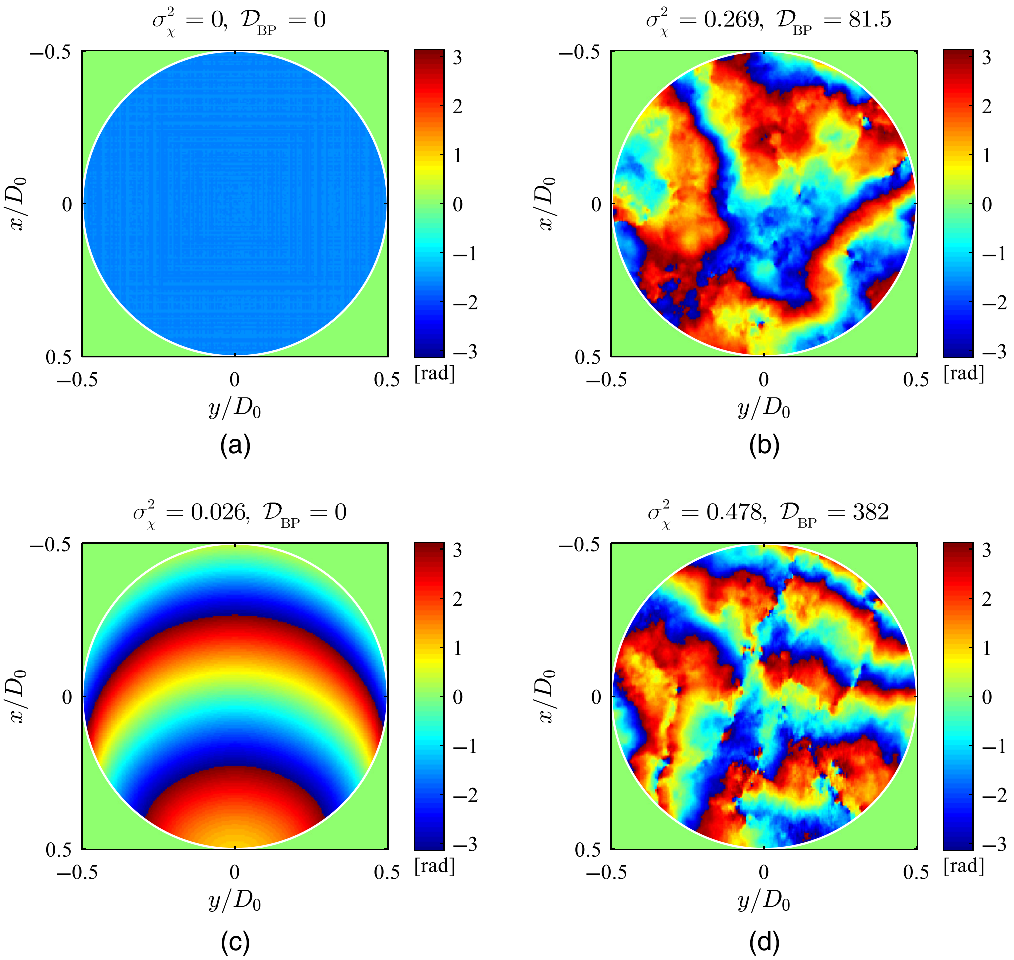

Fig. 5 Visualization of the backpropagated point-source beacon in the source plane. Here, we plot the wrapped phase associated with (a) the diffraction-limited case, (b) the turbulence-only case, (c) the TDTB-only case, and (d) the TTBI case. Similar to Figs. 4 and 6, we also report the log-amplitude variance σ_χ^2 and the branch-point density $\mathcal{D}_{BP}$ at the top of each subplot. Note that the white circles represent the initial diameter D_0.

small, and the bold curves are reasonably smooth. Thus, we will use the same number of Monte Carlo realizations in the analysis that follows.

4 Results and Discussion

This section contains results for the trade space setup in Sec. 2 and explored in Sec. 3. In particular, Fig. 8 shows results for the log-amplitude variance, σ_χ^2, and the branch-point density, $\mathcal{D}_{BP}$, both as a function of the number of wind-clearing periods N_{WCP} [cf. Eqs. (27), (28), and (12), respectively]. These metrics result from a point-source beacon being backpropagated from the target plane to the source plane through the simulated turbulence and TDTB. Here, we use N_{WCP} to help gauge when the time-dependent simulations reach steady state. From Fig. 8, we can see that both σ_χ^2 and $\mathcal{D}_{BP}$ overshoot and settle into steady state when $N_{WCP} \geq 0.5$. This outcome is consistent with Fig. 7. Note that in Fig. 8 the bold curves report the averages and the light curves report the standard deviations associated with 100 Monte Carlo realizations. Also note that the widths of these light curves are reasonably small, and the bold curves are reasonably smooth. Thus, we believe that 100 Monte Carlo realizations (i.e., the same number of realizations used in Part I of this two-part study) are adequate in quantifying the effects of TTBI.

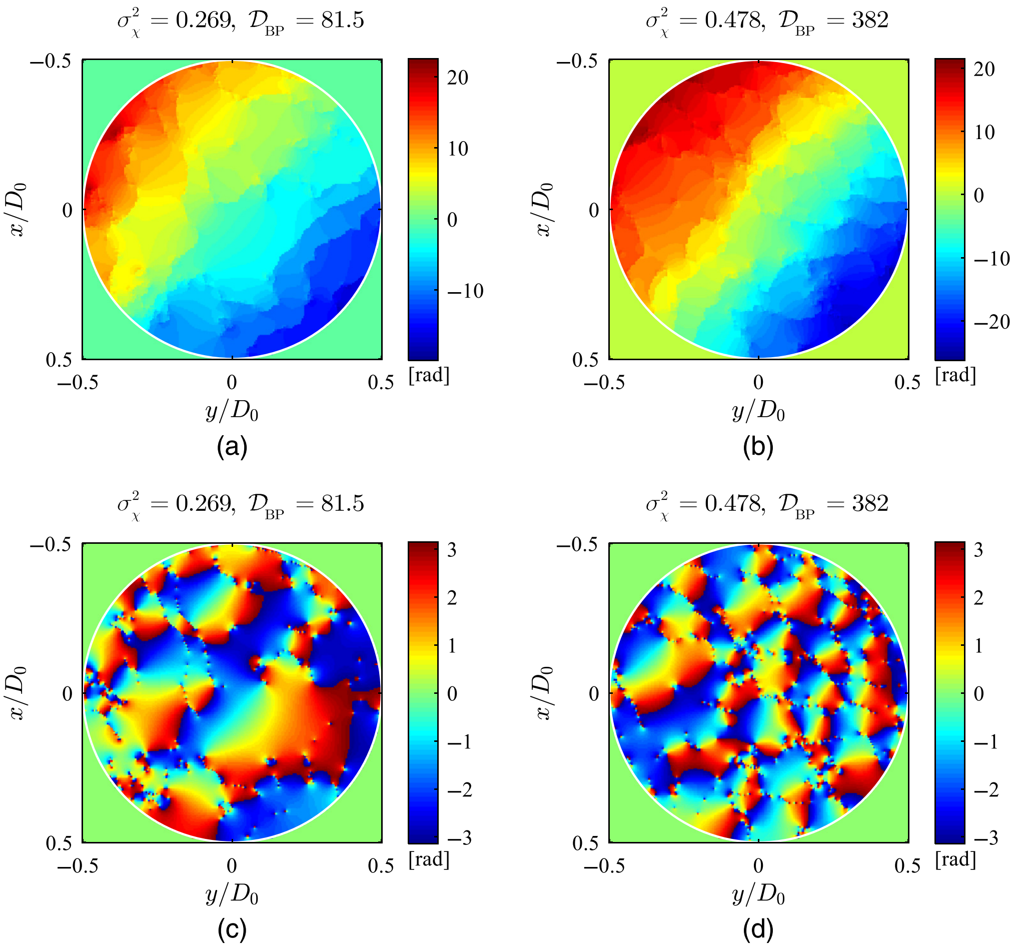

(a) (b) (c) (d)

Fig. 6 Visualization of the backpropagated point-source beacon in the source plane. Here, we plot the irrotational phase estimates for (a) the turbulence-only case and (b) the TTBI case, and the rotational phase estimates for (c) the turbulence-only case and (d) the TTBI case. Similar to Figs. 4 and 5, we also report the log-amplitude variance σ_χ^2 and the branch-point density $\mathcal{D}_{\mathrm{BP}}$ at the top of each subplot. Note that the white circles represent the initial diameter D_0.

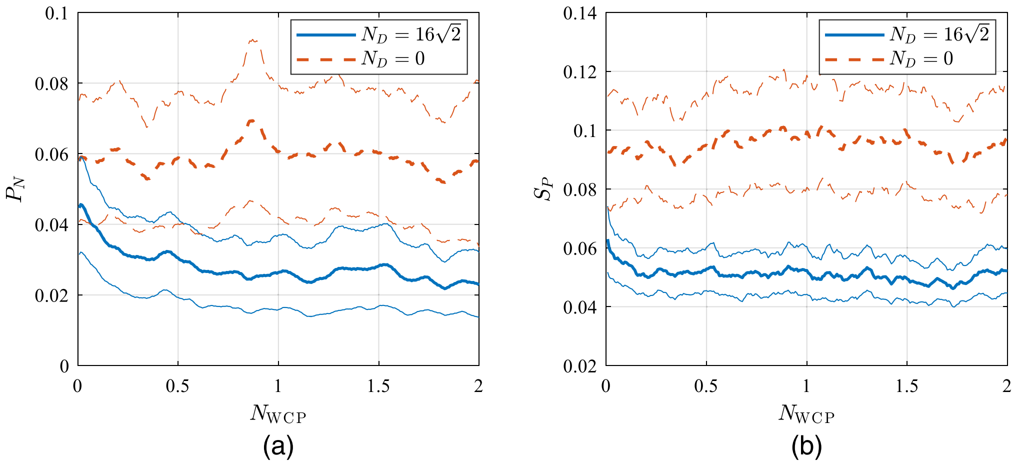

(a) (b)

Fig. 7 Visualization of the overall trade space in terms of the normalized PIB P_N and the peak Strehl ratio S_P: (a) P_N and (b) S_P. Note that we plot both metrics as a function of the number of wind-clearing periods N_{WCP}. Also note the bold curves represent the averages and the light curves represent the standard deviations associated with 100 Monte Carlo realizations.

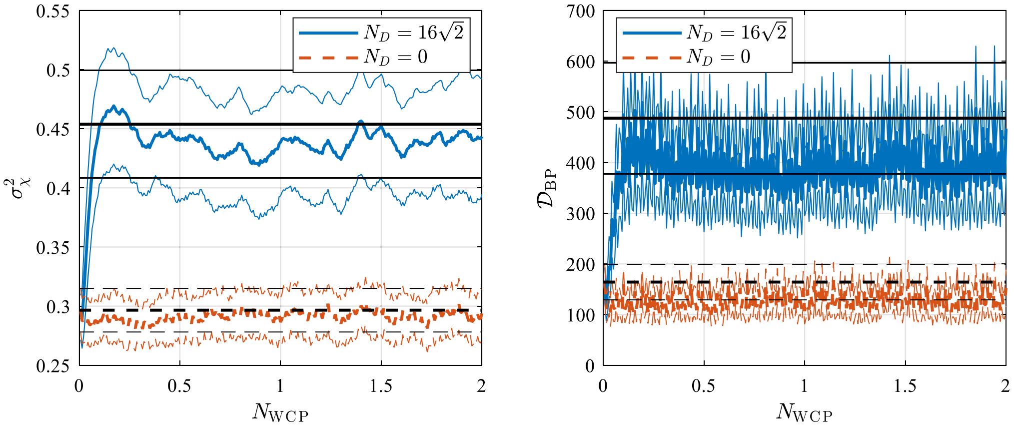

(a) (b)

Fig. 8 Results for the trade space setup in Sec. 2 and explored in Sec. 3: (a) the log-amplitude variance, σ^2_χ, and (b) the branch-point density, $\mathcal{D}_{\text{BP}}$, both as a function of the number of wind-clearing periods N_{WCP}. Here, the bold curves represent the averages and the light curves represent the standard deviations associated with 100 Monte Carlo realizations. It is important to note that the black-horizontal lines in (a) and (b) represent the averages (bold lines) and standard deviations (light lines) from simulating 100 Monte Carlo realizations of turbulence and SSTB (cf. Fig. 8 in Part I).

These results clearly show that TTBI results in an increased amount of scintillation when simulating turbulence and TDTB. For example, as shown in Fig. 8(a), the log-amplitude variance σ^2_χ had steady-state averages of 0.437 for the TTBI case (when $N_{\text{WCP}} \geq 0.5$), and 0.291 for the turbulence-only case (when $N_{\text{WCP}} \geq 0$). These steady-state averages agreed well with those obtained from simulating turbulence and SSTB [cf. the horizontal black lines in Fig. 8(a)], which had averages of 0.454 for the TTBI case (when $\mathcal{R}_{\text{sw}} = 0.25$ and $N_D = N_C = 16\sqrt{2} \approx 22.6$) and 0.297 for the turbulence-only case (when $\mathcal{R}_{\text{sw}} = 0.25$ and $N_D = 0$), leading to percentage errors of 3.88% and 1.92%, respectively.

The branch-point density $\mathcal{D}_{\text{BP}}$, as shown in Fig. 8(b), had steady-state averages of 390 for the TTBI case (when $N_{\text{WCP}} \geq 0.5$), and 127 for the turbulence-only case (when $N_{\text{WCP}} \geq 0$). These steady-state averages did not agree well with those obtained from simulating turbulence and SSTB [cf. the horizontal black lines in Fig. 8(b)], which had averages of 487 for the TTBI case (when $\mathcal{R}_{\text{sw}} = 0.25$ and $N_D = N_C = 16\sqrt{2} \approx 22.6$), and 164 for the turbulence-only case (when $\mathcal{R}_{\text{sw}} = 0.25$ and $N_D = 0$), leading to percentage errors of 24.8% and 29.3%, respectively. This lack of agreement was probably due to two phenomena. The first being due to the fact that TTBI does not allow the radians of distortion caused by TDTB to equal those caused by SSTB, and the second being due to the sensitivity of $\mathcal{D}_{\text{BP}}$ as a metric.[55] Both phenomena warrant further investigation (in subsequent papers). Nonetheless, the results presented in this paper clearly show that TTBI results in an increased amount of scintillation when simulating turbulence and TDTB.

With the above percentage errors in mind, the time-dependent assumptions contained in this paper ultimately allowed us to examine the Monte Carlo averages associated with the log-amplitude variance, σ^2_χ, and the branch-point density, $\mathcal{D}_{\text{BP}}$, with increased computational fidelity. However, this increased computational fidelity came at the expense of computational time. That is why we reserved the full trade space exploration to Part I of this two-part study. Relative to the time-dependent results contained in this paper, the steady-state results contained in Part I provide an upper bound on both the increase in σ^2_χ and $\mathcal{D}_{\text{BP}}$ due to TTBI (cf. Fig. 8 in both papers). It is our hope that such results will prove fruitful in the development of next-generation scaling laws that account for the effects of TTBI.[39–45]

5 Conclusion

In this paper, we used wave-optics simulations to look at the Monte Carlo averages associated with turbulence and TDTB. The goal throughout was to investigate TTBI. At a wavelength near

1 μm, TTBI increases the amount of scintillation that results from high-power laser beam propagation through distributed-volume atmospheric aberrations. In turn, to help gauge the strength of the simulated turbulence and TDTB, this paper made use of the following three parameters: the spherical-wave Rytov number, the number of wind-clearing periods, and the distortion number. These parameters simplified greatly, given a propagation path with constant atmospheric conditions. In addition, to help quantify the effects of TTBI, this paper made use of the following two metrics: the log-amplitude variance and branch-point density. These metrics resulted from a point-source beacon being backpropagated from the target plane to the source plane through the simulated turbulence and TDTB.

Overall, the results showed that TTBI causes the log-amplitude variance and the branch-point density to increase. These results pose a major problem for BC systems that perform phase compensation. In turn, the time-dependent simulations presented in this paper will provide much needed insight into the design of future systems.

Acknowledgments

The author of this paper would like to thank the Directed Energy Joint Transition Office for sponsoring this research, and C. E. Murphy for many insightful discussions regarding the results presented within.

References

1. C. B. Hogge, "Propagation of high-energy laser beams in the atmosphere," Technical Report AFWL-TR-74-74, Air Force Weapons Laboratory, Kirtland Air Force Base, New Mexico (1974). http://www.dtic.mil/dtic/tr/fulltext/u2/781763.pdf.
2. D. C. Smith, "High-power laser propagation: thermal blooming," *Proc. IEEE* **65**(12), 1679–1714 (1977).
3. J. L. Ulrich and P. B. Walsh, "Thermal blooming in the atmosphere," in *Laser Beam Propagation in the Atmosphere*, J. W. Strohbehn, Ed., Springer-Verlag, Heidelberg, New York (1978).
4. H. Weichel, *Laser Beam Propagation in the Atmosphere*, SPIE Press, Bellingham, Washington (1989).
5. F. G. Gebhardt, "Twenty-five years of thermal blooming: an overview," *Proc. SPIE* **1221**, 1–25 (1990).
6. N. M. Kroll and P. L. Kelley, "Temporal and spatial gain in stimulated light scattering," *Phys. Rev. A* **4**(2), 763–776 (1971).
7. T. J. Karr et al., "Perturbation growth by thermal blooming in turbulence," *J. Opt. Soc. Am. A* **7**(6), 1103–1124 (1990).
8. D. H. Chamber et al., "Linear theory of uncompensated thermal blooming in turbulence," *Phys. Rev. A* **41**(12), 6982–6991 (1990).
9. S. Enguehard and B. Hatfield, "Perturbative approach to the small-scale physics of the interaction of thermal blooming and turbulence," *J. Opt. Soc. Am A* **8**(4), 637–646 (1991).
10. R. Holmes, R. Myers, and C. Duzy, "A linearized theory of transient laser heating in fluid," *Phys. Rev. A* **44**(10), 6862–6876 (1991).
11. L. C. Bradley and J. Herrmann, "Phase compensation for thermal blooming," *App. Opt.* **13**(2), 331–334 (1974).
12. J. Herrmann, "Properties of phase conjugate adaptive optical systems," *J. Opt. Soc. Am.* **67**(3), 290–295 (1977).
13. T. J. Karr, "Thermal blooming compensation instabilities," *J. Opt. Soc. Am. A* **6**(7), 1038–1048 (1989).
14. J. R. Morris, "Scalar Green's-function derivation of the thermal blooming compensation instability equations," *J. Opt. Soc. Am. A* **6**(12), 1859–1862 (1989).
15. B. Johnson, "Thermal-blooming laboratory experiments," *Lincoln Lab. J.* **5**(1), 151–170 (1992).

16. J. F. Schonfeld, "Linearized theory of thermal-blooming phase compensation instability with realistic adaptive-optics geometry," *J. Opt. Soc. Am. B* **9**(10), 1803–1812 (1992).
17. J. R. Morris, J. A. Viecelli, and T. J. Karr, "Effects of a random wind field on thermal blooming instabilities," *Proc. SPIE* **1221**, 229–240 (1990).
18. J. F. Schonfeld, "The theory of compensated laser propagation through strong thermal blooming," *Lincoln Lab. J.* **5**(1), 131–150 (1992).
19. D. G. Fouche, C. Higgs, and C. F. Pearson, "Scaled atmospheric blooming experiments," *Lincoln Lab. J.* **5**(2), 273–293 (1992).
20. D. L. Fried and R. K. Szeto, "Wind-shear induced stabilization of PCI," *J. Opt. Soc. Am. A.* **15**(5), 1212–1226 (1998).
21. J. D. Barchers, "Linear analysis of thermal blooming compensation instabilities in laser propagation," *J. Opt. Soc. Am. A.* **26**(7), 1638–1653 (2009).
22. V. P. Lukin and B. V. Fortes, "The influence of wavefront dislocations on phase conjugation instability with thermal blooming compensation," *Pure Appl. Opt.* **6**(103) 256–269 (1997).
23. V. P. Lukin and B. V. Fortes, *Adaptive Beaming and Imaging in the Turbulent Atmosphere*, SPIE Press, Bellingham, Washington (2002).
24. M. F. Spencer et al., "Impact of spatial resolution on thermal blooming phase compensation instability," *Proc. SPIE* **7816**, 781609 (2010).
25. M. F. Spencer and S. J. Cusumano, "Impact of branch points in adaptive optics compensation of thermal blooming and turbulence," *Proc. SPIE* **8165**, 816503 (2011).
26. M. F. Spencer, "Branch point mitigation of thermal blooming phase compensation instability," MS Thesis, AFIT/OSE/ENP/11-M02, Air Force Institute of Technology, Wright Patterson Air Force Base, Ohio (2011). http://www.dtic.mil/dtic/tr/fulltext/u2/a538538.pdf.
27. D. L. Fried and J. L. Vaughn, "Branch cuts in the phase function," *J. Opt. Soc. Am. A* **31**(15), 2865–2881 (1992).
28. D. L. Fried, "Branch point problem in adaptive optics," *J. Opt. Soc Am. A* **15**(10), 2759–2768 (1998).
29. D. L. Fried, "Adaptive optics wave function reconstruction and phase unwrapping when branch points are present," *Opt. Commun.* **200**, 43–72 (2001).
30. T. M. Venema and J. D. Schmidt, "Optical phase unwrapping in the presence of branch points," *Opt. Exp.* **16**(10), 6985–6998 (2008).
31. M. J. Steinbock, M. W. Hyde, and J. D. Schmidt, "LSPV+7, a branch-point-tolerant reconstructor for strong turbulence adaptive optics," *App. Opt.* **53**(18), 3821–3831 (2014).
32. M. F. Spencer and T. J. Brennan, "Branch-cut accumulation using LSPV+7," in *Proc. OSA pcAOP*, p. PTh2D.2 (2017).
33. M. F. Spencer and T. J. Brennan, "Compensation in the presence of deep turbulence using tiled-aperture architectures," *Proc. SPIE* **10194**, 1019493 (2017).
34. G. A. Tyler, J. F. Belsher, and P. H. Roberts, "A discussion of some issues associated with the evaluation and compensation of thermal blooming," Technical Report TR-779, The Optical Sciences Company, Anaheim, California (1986).
35. P. H. Roberts, "Time development of thermal blooming," Technical Report TR-1574, The Optical Sciences Company, Anaheim, California (2002).
36. D. C. Zimmerman, "Wave optics simulation of thermal blooming," Technical Report TR-1771, The Optical Sciences Company, Anaheim, California (2008).
37. T. J. Brennan and P. H. Roberts, *AOTools the Adaptive Optics Toolbox for Use with MATLAB User's Guide Version 1.4*, The Optical Sciences Company, Anaheim, California (2010).
38. T. J. Brennan, P. H. Roberts, and D. C. Mann, *WaveProp a Wave Optics Simulation System for Use with MATLAB User's Guide Version 1.3*, The Optical Sciences Company, Anaheim, California (2010).
39. H. Breaux et al., "Algebraic model for CW thermal-blooming effects," *App. Opt.* **18**(15), 2638–2644 (1979).
40. R. J. Bartell et al., "Methodology for comparing worldwide performance of diverse weight-constrained high energy laser systems," *Proc. SPIE* **5792**, 76–87 (2005).
41. G. P. Perram et al., *Introduction to Laser Weapon Systems*, Directed Energy Professional Society, Albuquerque, New Mexico (2010).

42. N. R. Van Zandt, S. T. Fiorino, and K. J. Keefer, “Enhanced, fast-running scaling law model of thermal blooming and turbulence effects on high energy laser propagation,” *Opt. Exp.* **21**(12), 14789–14798 (2013).
43. S. A. Shakir et al., “General wave optics propagation scaling law,” *J. Opt. Soc. Am. A* **33**(12), 2477–2484 (2016).
44. S. A. Shakir et al., “Far-field propagation of partially coherent laser light in random mediums,” *Opt. Exp.* **26**(12), 15609–15622 (2018).
45. P. H. Merritt and M. F. Spencer, *Beam Control for Laser Systems*, 2nd ed., Directed Energy Professional Society, Albuquerque, New Mexico (2018).
46. C. E. Murphy and M. F. Spencer, “Investigation of turbulence thermal blooming interaction using the split-step beam propagation method,” *Proc. SPIE* **10772**, 1077208 (2018).
47. A. Fleck, Jr., J. R. Morris, and M. D. Feit, “Time-dependent propagation of high energy laser beams through the atmosphere,” *Appl. Phys.* **10**, 129–160 (1976).
48. A. Fleck, Jr., J. R. Morris, and M. D. Feit, “Time-dependent propagation of high energy laser beams through the atmosphere: II,” *Appl. Phys.* **14**, 99–115 (1977).
49. N. R. Van Zandt et al., “Polychromatic wave-optics models for image-plane speckle. 1. Well-resolved objects,” *App. Opt.* **57**(15), 4090–4102 (2018).
50. N. R. Van Zandt et al., “Polychromatic wave-optics models for image-plane speckle. 2. Unresolved objects,” *App. Opt.* **57**(15), 4103–4110 (2018).
51. J. D. Schmidt, *Numerical Simulation of Optical Wave Propagation using MATLAB*, SPIE Press, Bellingham, Washington (2010).
52. G. R. Osche, *Optical Detection Theory for Laser Applications*, John Wiley & Sons, Hoboken, New Jersey (2002).
53. L. C. Andrews and R. L. Phillips, *Laser Beam Propagation through Random Media*, 2nd ed., SPIE Press, Bellingham, Washington (2005).
54. R. J. Sasiela, *Electromagnetic Wave Propagation in Turbulence Evaluation and Application of Mellin Transforms*, 2nd ed., SPIE Press, Bellingham, Washington (2007).
55. J. R. Beck et al., “Investigation of branch-point density using traditional wave-optics techniques,” *Proc. SPIE* **10772**, 1077206 (2018).

Mark F. Spencer is a senior research physicist and the principal investigator for Aero Effects and Beam Control at the Air Force Research Laboratory, Directed Energy Directorate. In addition, he is an adjunct assistant professor of optical sciences and engineering at the Air Force Institute of Technology (AFIT), within the Department of Engineering Physics. He received his PhD in optical sciences and engineering from AFIT in 2014. He is a senior member of SPIE.